Electromagnetic Applications in Methane Hydrate Reservoirs

6

Katrin Schwalenberg and Marion Jegen

Abstract

Marine electromagnetic methods provide useful and independent measures for the identification and quantification of submarine gas hydrates. The resistivity of seafloor sediments, drawn from area-wide electromagnetic data, mainly depends on the sediment porosity and the nature of the pore fluid. Gas hydrates and free gas are both electrically resistive. The replacement of saline water, thus conductive pore water with resistive gas hydrate or free gas, increases the sediment resistivity and can be used to provide accurate saturation estimates if the background lithology is known. While seismic methods are predominantly used to study the distribution of submarine gas hydrates, a growing number of global field studies have demonstrated that the joint interpretation of marine seismic and electromagnetic methods improves the evaluation of submarine gas hydrate targets. This article discusses the relationship between resistivity and free gas/gas hydrate saturation levels, how the resistivity of the sediment may be measured and summarizes the status and results of current and past field studies.

6.1 Introduction

The exploration of submarine gas hydrate deposits demands robust methods and survey designs that address certain fundamental questions, including: (a) where do gas hydrates occur? (b) how can they be identified? (c) how are they distributed within the gas hydrate stability zone (GHSZ)? (d) what are the properties of the surrounding sediment? (e) and what are the gas hydrate saturation levels? Answering these questions requires geophysical methods that are sensitive to the physical properties of gas hydrates and have penetration depths covering the entire GHSZ. Next to seismic methods, marine electromagnetic methods and controlled source electromagnetic (CSEM) methods in particular have provided some of the most important insights into the sub-seafloor gas hydrate distribution, having been used globally since first considered by Edwards (1997).

Marine electromagnetic methods are complementary to seismic methods on various levels. The most important complementary data from these two methods allow for the differentiation between the impact of methane hydrates and gas on the physical properties of electrical resistivity and seismic velocity. Electrical resistivity increases when gas hydrates and/or free gas are present in the pore space of sediment. The compressional velocity also increases with higher gas hydrate saturation levels, but decreases if free gas is present in the pore space. This leads to the characteristic amplitude reversal at the base of the hydrate stability zone known as the bottom simulating reflection (BSR). Shear wave velocities, on the other hand, are only affected by gas hydrates and not by free gas. Deriving electrical resistivity models together with a reflection seismic section and velocity models therefore put spatial constraints on the electrical resistivity distribution, allowing for the distinction of free gas and hydrate saturation levels in the sediment.

Differences in the resolution capabilities of these two methods also make them well-suited for cooperative evaluation. Reflection seismic data allow for the delineation of structures associated with hydrate occurrences at high resolution. Seismic images of chimneys and faults (representing the conduits and pathways that free gas and gas-charged fluids use to migrate into the GHSZ, forming gas hydrate deposits) and high amplitude reflections may indicate local gas hydrate accumulations. Such high-resolution imaging is

K. Schwalenberg (✉)
BGR - Federal Institute for Geoscience and Natural Resources, Hannover, Germany
e-mail: katrin.schwalenberg@bgr.de

M. Jegen
GEOMAR - Helmholtz Centre for Ocean Research Kiel, Kiel, Germany

not possible with CSEM data due to the diffusive nature of low frequency electromagnetic field propagation. However, the seismically-derived structures may be implemented a-priori to sharpen boundaries when deriving the electrical resistivity model.

This article discusses the effects of gas hydrates and free gas on the electrical properties of sediment, and how hydrate/free gas concentration estimates can be derived from electrical resistivity models. We cover the general concept of marine CSEM, which is the preferred method for deriving the electrical resistivity model for hydrate exploration. Before moving on to two examples of field surveys in the last section, we provide an overview of the heterogeneous types of electromagnetic instrumentation developed at different academic institutions for hydrate exploration over the last two decades.

6.2 Electrical Properties of Gas Hydrates

While seismic velocity is governed by properties of the rock matrix, electrical resistivity yields a measure of the pore fluid. The rock matrix of the sediment has a very high level of resistivity, with the main electrical conduit occurring through the movement of ions in the pore fluid. The bulk electrical resistivity (or its reciprocal electrical conductivity) of marine sediment is, therefore, primarily a function of sediment porosity, permeability and the resistivity of the pore fluid, which decrease with an increase in salinity and ion content. The replacement of conductive pore fluid by resistive constituents such as gas hydrates or free gas increases the bulk resistivity. The experimentally derived Archie's equation (Archie 1942) is commonly used to calculate the formation resistivity ρ_{bulk} given the porosity ϕ and pore fluid resistivity ρ_{fluid}

$$\rho_{bulk} = a\phi^{-m}\rho_{fluid}S^{-n} \qquad (6.1)$$

where a and m are empirically derived coefficients from sources such as borehole data or laboratory measurements on sediment samples. Typical values for a are in the range of 0.9–1.1 (theoretically 1.0 at 100% porosity, Winsauer et al. 1952), with m varying between 1.4 and 2.2 for marine sediment (Cook and Waite 2018). The sediment porosity ϕ may be provided from drilling, core samples, or seismic velocity and electrical resistivity data of hydrate/gas-free background lithologies. The pore fluid resistivity ρ_{fluid} is a function of salinity, temperature and pressure (e.g., Fofonoff 1985; McDougall and Barker 2011) and is often assumed to equal the seawater resistivity, measured by a conductivity-temperature-depth probe close to the seafloor. The saturation S denotes the fraction of pores space filled with pore water and is 1.0 for hydrate- and gas-free marine sediment. Accordingly, the gas hydrate or free gas saturation level can be derived setting $S_h = (1 − S)$ with the empirical saturation exponent n in Eq. (6.1). Pearson et al. (1983) presented an average saturation exponent of $n = 1.9386$ for gas hydrates, which has been frequently used for borehole- and CSEM-derived gas hydrate saturation level estimates (e.g., Collett and Ladd 2000; Tréhu et al. 2006; Weitemeyer et al. 2011). Theoretically, n may vary in the range of 0.5–4.0 (Spangenberg 2001), depending on porosity, grain size, grain distribution and saturation itself. The saturation exponent was recently revised by Cook and Waite (2018), who suggest using $n = 2.5 \pm 0.5$ in the absence of independent estimates.

6.2.1 Saturation Estimates

The accuracy of saturation estimates using Archie's Eq. (6.1) depends on appropriate assumptions of the coefficients a, m and n, as well as about the porosity and pore water resistivity. This requires the availability of porosity profiles from seismic data, compaction trends, temperature gradients, pore water salinity data, or (for the most precise results) physical constraints derived from nearby borehole data. Also, if the presence of clay is not considered, it may lead to deviations from Archie's equation and thus false saturation estimates (e.g., Jackson et al. 1978; Worthington 1993; Salem and Chilingarian 1999). Correction methods for incorporating clay content have been suggested by Lee and Collett (2006) and Sava and Hardage (2007), among others. In the absence of any other constraints, first order saturation estimates can be derived from anomalous resistivities normalized by the background resistivity profiles of hydrate-free zones, assuming similar lithologies (Schwalenberg et al. 2005).

The importance of being able to constrain the input parameter of Archie's equation is outlined in Fig. 6.1, which shows equivalent solutions for constant bulk sediment resistivity as a function of porosity, saturation and cementation factor m. The figure demonstrates that for low resistivities close to typical seafloor sediment resistivities (i.e., 1 and 3 Ωm), there is in theory a wide solution space in terms of reasonable porosity, cementations factor and saturation values. Thus, accurate free gas/hydrate saturation estimates in the realm of only slightly elevated bulk resistivities require a good knowledge of porosity and m. For high resistivities, the solution space is reduced and thus the associated high saturation values can be determined more accurately.

As emphasized above, the presence of free gas within the GHSZ also increases the bulk resistivity but decreases seismic velocities, which may result in disparities between saturation estimates from electrical resistivity and velocity data. Under
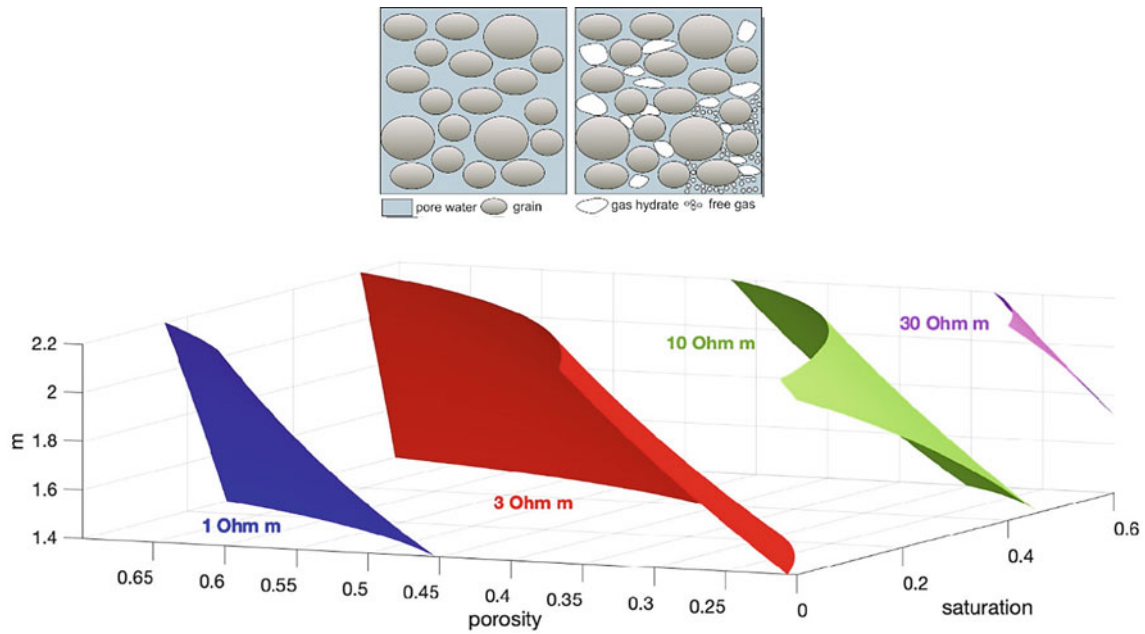
Fig. 6.1 Upper panels show the schematics of two-phase high porosity sediment (left). Electrical conduction occurs through ions in the pore water. Right panel shows a schematic for reduced pore space filled with gas hydrates and free gas. Lower panel shows equivalent solutions of Eq. (6.1) for constant bulk resistivities of 1, 3, 10, and 30 Ωm, respectively, in terms of porosity, saturation level and cementation factor m, setting $a = 1$ and $n = 2$

normal conditions, gas hydrates will form within the GHSZ if gas and water are available beyond the solubility limit of gas in water. In tectonically active areas, free gas may migrate high up into the GHSZ along faults and chimneys, if the gas supply and pressure are high enough. Such features have distinct acoustic patterns such as local high amplitude reflections and blanking, which can be recognized in reflection seismic profiles (e.g., Riedel et al. 2002; Liu and Flemings 2006; Bünz et al. 2012; Crutchley et al. 2015). The joint analysis of resistivity data, seismic reflection and velocity data along with borehole data therefore reduces ambiguities in the interpretation, yielding information on how hydrates are distributed within the sediment matrix (Ellis et al. 2008b) and leading to more accurate hydrate saturation level estimates (Attias et al. 2020).

6.3 Marine CSEM Principle

The marine CSEM method is based on the diffusive propagation of electromagnetic (EM) signals, which are generated by an electric or magnetic source dipole on or close to the seafloor, and the response signal of the ground recorded by electric or magnetic receiving dipoles, which can also be placed on the seafloor or towed behind the source dipole (e.g., Ward and Hohmann 1988; Edwards 2005; Constable 2010). EM field propagation follows the principle of EM induction, where time-varying EM fields generate eddy

currents in a conductive media; in this case that media is the surrounding seawater and the seafloor (e.g., Nabighian 1991). Note that in terrestrial cases air is non-conductive, and induction can only take place in the ground.

EM fields are attenuated and phase shifted while propagating outwards from the source. These effects are functions of the surrounding resistivity, thus containing information about the seafloor. Attenuation also limits the penetration depth (i.e., the depth window), which may be investigated. A simple formula used to calculate the penetration depth is $\delta = 500 \ (\rho/f)^{1/2}$ (e.g., Nabighian 1991), which denotes the depth in meters where the amplitude of the source signal at frequency f or time $T = 1/f$ is reduced by a factor of 1/e in a homogeneous medium of resistivity ρ. Within this depth window, the resolution is highest for shallow regions using high frequency or early time data and decreases with sediment depth, where lower frequencies or late times are required to generate measurable signals. An increase in the dipole moment of the source (length and current amplitude for an electric source dipole, number of loops, area and current amplitude for a magnetic source dipole) increases the amplitude of the source signal and thus the signal-to-noise ratio of the received signal, such that higher frequencies and earlier time signals at larger offsets can be recorded. This may counteract the resolution problem to a certain degree. An increase in resolution is also achieved by generating multiple frequency signals with the transmitter through appropriate current patterns in the electric or magnetic

source dipole. The current propagation and the recorded data can be analyzed in either the time domain or the frequency domain (Avdeeva et al. 2007; Connell and Key 2013).

Figure 6.2 displays the propagation in time of EM fields generated by a horizontal electric source dipole placed on a uniform seafloor (left) and a model with a 3D resistive target included (right). EM fields are attenuated outwards from the source, decaying faster in the conductive upper layer representing the ocean than in the lower resistive seafloor. The 3D resistive target causes higher field amplitudes arriving at earlier times on the seafloor at distance from the source dipole.

6.4 CSEM Data Interpretation

CSEM data interpretation requires the identification of a resistivity model to explain the measured data. This is typically performed by numerical modeling and inversion. The derivation of a discrete electrical resistivity model from CSEM data is (as most geophysical problems) an ill-posed problem, as the measured data are digitized and discrete point measurements are each associated with an error. Thus, a solution to the inverse problem is non-unique and an arbitrary number of models may predict data that fit the measured data within the error.

Further ambiguity arises from the fact that the physics of the EM method preclude the resolution of independent parameters. For example, a thicker, less resistive layer may generate the same model response as a thinner, more resistive layer. Both are equivalent models explaining the data and only the resistivity-thickness product of the layer can be resolved. Generally in marine EM, the upper boundary of a resistive anomaly such as a hydrate/free gas target is usually well constrained, while the lower boundary may be more poorly resolved. Lateral contrasts can also be accurately resolved depending on data coverage, depth and complexity of the target.

Iterative inversion schemes are commonly used to derive a resistivity model from the data. In an iterative scheme, a starting resistivity model is altered iteratively until the predicted response of the model fits the observed data within the error. The iterative inversion process is stabilized by including a regularization term in the least square formulation of the objective function (Tikhonov and Arsenin 1977). Given the diffusive nature of EM field propagation, a commonly used procedure is to apply a weighted roughness penalty term with the aim to find the optimum minimum
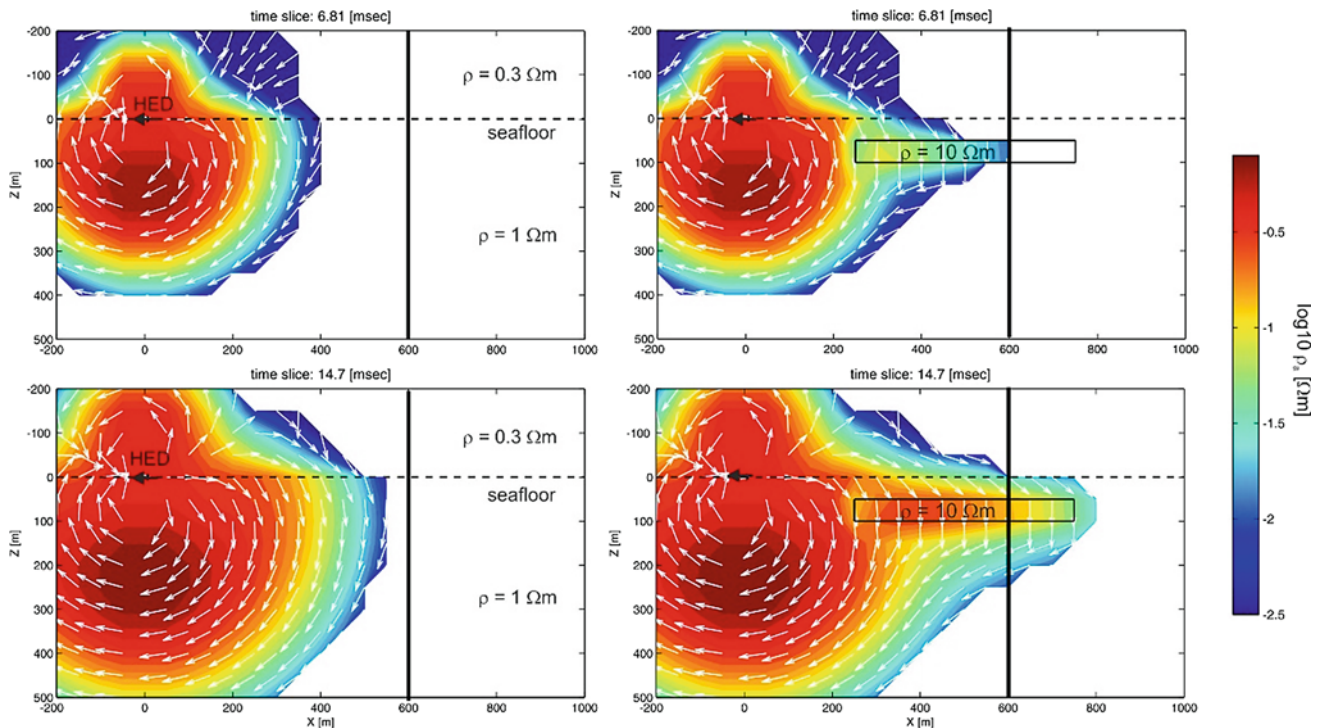

Fig. 6.2 Electromagnetic propagation of a horizontal electric dipole (HED) on the seafloor, left for a uniform seafloor resistivity model of 1 Ωm, right with a resistive 3D body (10 Ωm, 50 m thickness at 50 m below seafloor), simulating a gas hydrate deposit for two steps in time (top and bottom rows). Electromagnetic energy decays outwards with time and is clearly biased by the resistive block, causing higher electric field amplitudes and earlier arrival times at the seafloor where measurements are taken. Arrows show the direction of the total electric field in the x–z plane and colors show the total electric field normalized with the DC current density, which corresponds to the apparent resistivity of the total field

structure model that fits the data (Occam-type inversion, Constable et al. 1987), which has become the standard in EM data interpretation. A drawback of the methodology is that due to the non-linear nature of the problem, the resulting model may depend on the starting model. For 2D marine EM data interpretation, we mention the open-source code MARE2DEM by Key (2016).

Another class of tools used for interpretation are Bayesian inversion methods, which randomly search the solution space using Monte Carlo-type methods, providing statistically derived measures of model uncertainties without the assumption of linearity between model and data spaces (i.e., Ray et al. 2013; Gehrmann et al. 2016). Due to the computational costs, the use of Bayesian methods have been limited to 1D marine EM problems, while Occam inversion is the standard in 2D and forthcoming in 3D inversions.

Both regularized and statistical approaches allow the incorporation of a-priori information into the inversion process (i.e., layer boundaries from seismic sections or resistivity constraints from borehole data). This helps to constrain the number of possible models and to find joint solutions explaining all available data but may also add bias to the model-finding process.

6.5 CSEM Instrumentation and Exploration History

A variety of EM survey methods have been adapted or developed for the area-wide exploration of submarine gas hydrates. Here we provide an overview of those survey layouts that have been used in field studies published in the literature. Sketches of the described survey configurations are shown in Fig. 6.3.

6.5.1 Seafloor-Towed Systems

The use of marine CSEM for the exploration of submarine gas hydrates was first suggested by Edwards (1997) in the late 1990s. He proposed the use of a seafloor-towed electric dipole–dipole system and an analysis in time domain. A system with a ∼100 m long transmitting dipole and two receiving dipoles at adjustable offsets between 170 and 385 m was developed and used for gas hydrate studies on the Cascadian Margin offshore Vancouver Island (Yuan and Edwards 2000; Schwalenberg et al. 2005; Gehrmann et al. 2016), offshore Chile (Schwalenberg et al. 2004) and on the Hikurangi Margin of New Zealand (Schwalenberg et al. 2010) (see also Fig. 6.4 for locations of global marine CSEM studies). An advanced seafloor-towed system (HYDRA) with up to five electric receiving dipoles at offsets between 150 and 850 m from the 100 m source dipole has been used to study gas hydrates on the Hikurangi margin (Schwalenberg et al. 2017), and in the offshore Danube Fan of the western Black Sea (Schwalenberg et al. 2020). The target depths of these systems reach from seafloor to 200–500 m below, depending on transmitter receiver offsets and the bulk resistivity of the seafloor.

A seafloor-towed magnetic dipole–dipole system with a total length of 50 m and three receivers at offsets of 4, 13 and 40 m from the magnetic source (Evans 2007) was used
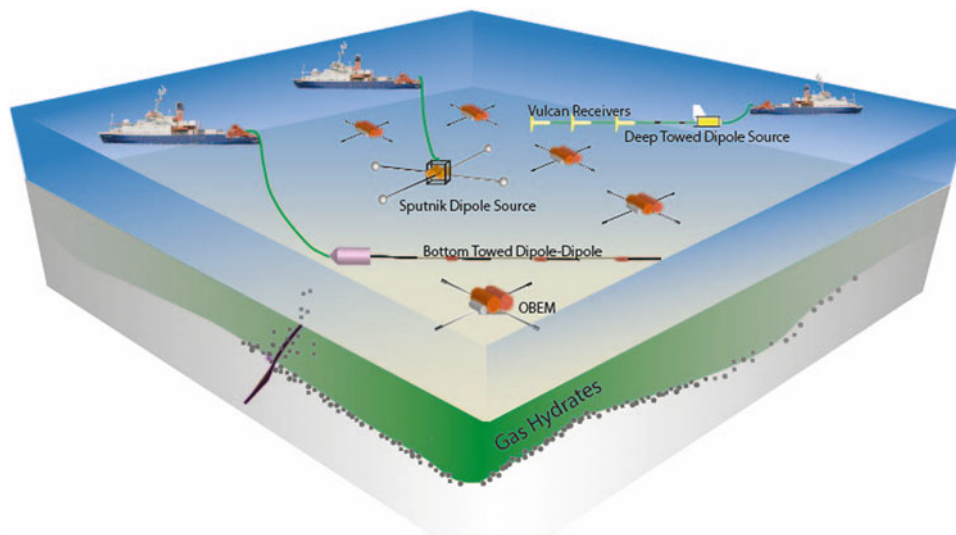

Fig. 6.3 Sketch of possible marine electromagnetic survey layouts. Exemplarily shown are the seafloor-towed electric dipole–dipole system (i.e., HYDRA) and the deep-towed horizontal electric dipole transmitter (i.e., SUESI/DASI with VULCAN receivers), which are 2D profiling methods. Deep-towed dipole sources and the perpendicular dipole seafloor transmitter (SPUTNIK) used in conjunction with stationary ocean bottom electromagnetic receivers (OBEMs), are appropriate for 3D CSEM exploration. References are provided in the text
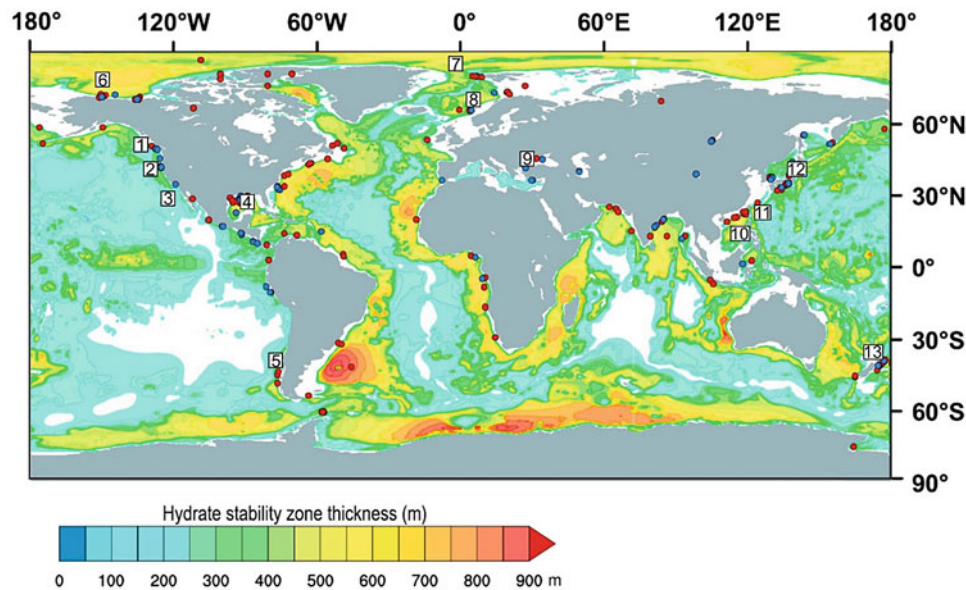
Fig. 6.4 Overview of marine CSEM gas hydrate surveys to date (numbers in squares). The underlying map by Ruppel and Kessler (2017) shows the thickness of the theoretical GHSZ by Kretschmer et al. (2015) with locations of known (blue circles) and inferred (red circles) gas hydrate occurrences by Ruppel and Kessler (2017). (1) Cascadia Margin: Yuan and Edwards (2000), Schwalenberg et al. (2005), Mir and Edwards (2011), Gehrmann et al. (2016), (2) Hydrate Ridge: Weitemeyer et al. (2006, 2011); (3) Outer California Borderlands: Kannberg and Constable (2020); (4) Northern Gulf of Mexico: Ellis et al. (2008a); Weitemeyer and Constable (2010), Weitemeyer et al. (2017); (5) Chile Margin: Schwalenberg et al. (2004); (6) Beaufort Shelf, Alaska: Sherman et al. (2017); (7) Vestnesa Ridge and Svalbard Margin: Goswami et al. (2015; 2016); (8) Norway: Attias et al. (2016, 2018); (9) Western Black Sea: Schwalenberg et al. (2020); Duan et al. (2020); (10) South China Sea: Jing et al. (2019); Wang et al. (2019); (11) SW Taiwan Sea: Hsu et al. (2014); Jegen et al. (2014); (12) Japan: Goto et al. (2008); OFG (2014, 2015, 2018); (13) Hikurangi Margin, New Zealand: Schwalenberg et al. (2010, 2017)

to study gas hydrates in deep-water seafloor mounds in the northern Gulf of Mexico (Ellis et al. 2008a), and gas hydrate targets offshore southwest Taiwan (Hsu et al. 2014). The system focuses on the shallow seafloor, reaching down to depths of 20–30 m below seafloor, but in principle can be extended to greater depths.

Seafloor-towed systems are obviously limited to smooth, sediment-covered seafloor conditions, which are generally found at the continental slope regions where most gas hydrate studies take place. In regions where the seafloor is protected or occupied by seafloor infrastructure, the deployment of seafloor-towed systems may be prohibited. While seafloor-towed measurements minimize signal loss in the ocean layer by directly coupling to the seafloor, measurement progress is slow, typically in the order of 0.5–1.0 knots. The advantage of seafloor-towed systems is that transmitter–receiver offsets, which needs to be accurately identified for the data analysis, do not change during surveying and do not require complex navigation procedures. Only the layback of the instrument to the vessel is measured acoustically. Data quality is usually very high at much lower source signal amplitudes ($\sim$10–20 A) compared to deep-towed transmitter sources ($\sim$100–500 A). Areas of interest can be surveyed in higher resolution by stopping the array and increasing the stacking depth at shorter intervals.

6.5.2 Deep-Towed Systems

Ocean bottom electromagnetic (OBEM) receivers have been used for passive magnetotelluric studies of the oceanic crust and mantle for many decades (e.g., Filloux 1987; Baba 2005, and references therein). The development of deep-towed transmitters with a horizontal electric dipole antenna, used to collect CSEM data in conjunction with stationary OBEM receivers, pushed applications towards shallower target depths from seafloor to 1–2 km below (Sinha et al. 1990; Flosadottir and Constable 1996; Constable 2013). This has opened the door for application in the offshore hydrocarbon exploration industry (e.g., Ellingsrud et al. 2002; Edwards 2005; Constable 2010). OBEM receivers are placed on the seafloor along profiles or on a grid and the CSEM source with dipole lengths of 50–200 m is towed at 50–100 m above seafloor over the survey area. The source signal typically has a square waveform with a fundamental frequency around 1 Hz or of multiple frequency content (Myer et al. 2011), and amplitudes in the order of 100–500 A or even higher for industry applications. The configuration has been used to study gas hydrates at Hydrate Ridge offshore Oregon (Weitemeyer et al. 2011), the northern Gulf of Mexico (Weitemeyer et al. 2017) and in the South China Sea (Wang et al. 2015).

On one hand, this set-up has much higher operational costs and faces more logistic efforts compared to the seafloor-towed systems. Elaborate navigation procedures are required to obtain accurate transmitter and receiver positions for the data analysis (Weitemeyer et al. 2011; Key and Constable 2021), and small-scale, shallow targets may therefore be overlooked due to the saturation of receiver data at short offsets (Attias et al. 2018).

On the other hand, larger survey areas can be covered using comparable ship time. Both, inline and broadside data of the electric and magnetic fields are recorded, which provide 3D information of the sub-seafloor electrical structure if the receivers are deployed in a grid. Magnetotelluric data recorded before or after the CSEM survey provide constraints of the deeper seafloor and can be included in the analysis. Further, deeper targets can be surveyed at greater offsets, and measurements can be carried out in areas with seafloor infrastructure without risking damage or loss of instrumentation.

A recent advancement in this setup is the development of three-component electric field receivers (VULCAN, Constable et al. 2016), which are deep-towed at fixed offsets behind the CSEM transmitter antenna. The data can be jointly analyzed with the OBEM data, which significantly improves target resolution. A combination of one or more Vulcan receivers and OBEM receivers have been used to study gas hydrate targets at Vestnesa Ridge west of Svalbard (Goswami et al. 2015), at the Svalbard continental slope (Goswami et al. 2016) in the central Norwegian margin (Attias et al. 2018) and at the outer California Borderlands (Kannberg and Constable 2020).

A special case of a deep-towed system is the marine DC resistivity system (MANTA, Goto et al. 2008). It consists of a deep tow transmitter package (with a 20 A current amplitude) followed by a buoyant, ~160 m long streamer with seven current dipoles that vary in length from 20 to 100 m, and offsets from 65 to 132 m from the receiving dipole. The system has been used to study gas hydrate targets in the Japan Sea, and is sensitive down to ~100 m below seafloor (Goto et al. 2008).

6.5.3 Other Systems

Two other unique CSEM experiments are mentioned, although they do not fit into the classifications of the previous section.

A stationary seafloor electric dipole–dipole system was installed at the Bullseye node of the Neptune Canada Observatory at Cascadia, offshore Vancouver Island (Mir and Edwards 2011). It monitored the CSEM data of the local gas hydrate system over a period of ~2 years before it was removed from the observatory. The system consisted of a seafloor transmitter with a 95 m long dipole antenna and five receiving units, which were distributed in 200 m offsets. Unfortunately, only one of these receivers managed to collect useful data (Mir 2011).

Duan et al. (2021) have described a small-scale, high-resolution 3D CSEM experiment using a transmitter package with two 10 m long horizontal dipoles (SPUTNIK), which allow transmissions at 20 A in two orthogonal directions at the same location. The cable-connected transmitter is moved from site to site over a 3D array of OBEM receivers. As relative positioning between transmitter and receiver locations is important at short offsets, direct distance measurements are performed using acoustic systems mounted to both the transmitter and the receivers.

6.6 Global Case Studies

The locations of published marine CSEM gas hydrate field studies to-date are plotted on the map in Fig. 6.4, along with the measured thicknesses of the GHSZ under present day climate conditions by Kretschmer et al. (2015), and known and inferred gas hydrate findings by Ruppel and Kessler (2017). Our compilation of CSEM studies may not be entirely complete but should nevertheless cover most field studies carried out to-date. Assuming that seismic studies exist for most of the submarine gas hydrate sites in Fig. 6.4, this reveals a demand for further CSEM gas hydrate studies on a global level.

We focus here on two case studies from our own work and refer the reader to the referenced literature in Fig. 6.4. The seafloor-towed electric dipole–dipole system previously described was used in both case studies.

The first case study is from the Hikurangi Margin off the east coast of New Zealand's North Island. The Hikurangi Margin is characterized by the westward subduction of the Pacific plate beneath the Indo-Australian plate. Approximately 500–2000 m of thick, water-rich sediment lie on top of the 12–15 km thick oceanic crust of the Hikurangi Plateau (e.g., Barnes et al. 2010). The presence of gas hydrates has been inferred from widespread bottom simulating reflections (Lewis and Marshall 1996; Henrys et al. 2003; Pecher et al. 2004) and through the direct sampling of gravity cores (Bialas et al. 2007; Bialas 2011). Evidence derived from seep fauna reveal that methane seepage is abundant along the margin, giving rise to thick carbonate crusts, bacteria mats, and gas bubble plumes that reach several hundred meters into the water column (Lewis and Marshall 1996).

Figure 6.5a. shows the CSEM results derived from the 2D inversion of a profile at Opouawe Bank, located at the southern end of the Hikurangi margin (Schwalenberg et al. 2017). The profile intersects with several sites of intense gas seepage from the seafloor (Greinert et al. 2010; Klaucke
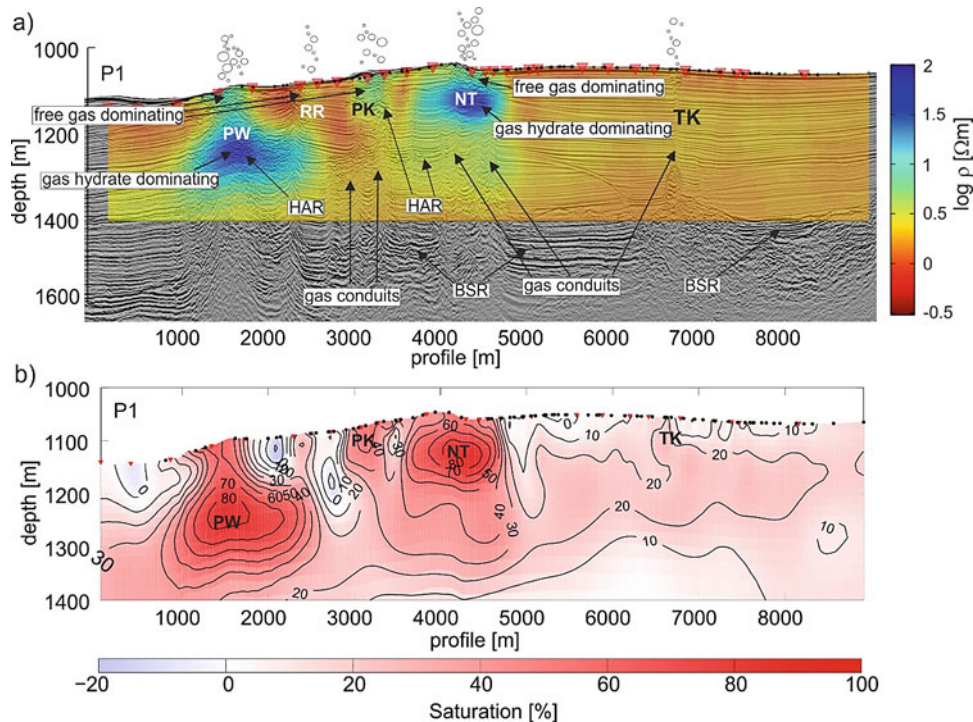
Fig. 6.5 **a** Resistivity model derived from the 2D inversion of CSEM data from the Hikurangi Margin, offshore New Zealand (Schwalenberg et al. 2017) overlaid on the 2D MCS section (Koch et al. 2016). The profile intersects several seafloor vent sites named Piwakawaka (PW), Riroriro (RR), Pukeko (PK), North Tower (NT) and Takahe (TK). Model parts deeper than 1400 mbsf have low sensitivity and have been cut. **b** Gas hydrate saturation model derived from the above resistivity model using Archie's equation with a linear porosity gradient from 58% at the seafloor to 50% at 300 mbsf, a pore water resistivity model derived from bottom seawater conductivities, local heat flow and seafloor temperatures and Archie coefficients $a = 1$, $m = 2.4$, and $n = 2$. Red triangles and black dots mark transmitter and receiver dipole positions, respectively. HAR: high amplitude reflections, BSR: bottom simulating reflections. (Figure was modified from Schwalenberg et al. 2017)

et al. 2010). Zones of highly anomalous resistivities (>50 Ωm, blue colors) occur at intermediate depths within the GHSZ below two seep sites (Piwakawaka and North Tower, see figure caption for abbreviations of seep names). Resistivities are less anomalous (3–10 Ωm) at the shallow depths below Riroriro and Pukeko. Seep site Takahe reveals only a very minor CSEM signature. Outside of the seep areas, the resistivities exhibit background values of 1–2 Ωm for marine water-saturated sediment.

The resistivity model is overlaid on the coincident 2D multichannel seismic (MCS) reflection profile (Koch et al. 2016). The seismic image shows several gas conduits below the seeps, which are characterized by high amplitude reflections (HAR), blanking and acoustic turbidity. The BSR is discontinuous in these parts, which points to significant gas pressure from below, transporting gas bubbles into the GHSZ. Outside the seep areas, the seismic section reveals horizontal strata. The areas of highest resistivity at intermediate depth below the seeps are interpreted to be dominated by gas hydrates; free gas may prevail at shallower

depths, supporting active seafloor venting (Schwalenberg et al. 2017).

The gas hydrate saturation estimates in Fig. 6.5b were calculated from the resistivity model using Archie's Eq. (6.1). In the absence of nearby borehole data, a porosity profile (58–50% from seafloor to 300 m below) was interpolated from gravity cores and a pore-water resistivity profile from bottom seawater resistivities and local thermal gradients (0.31–0.24 Ωm from seafloor to 300 m below), with Archie coefficients from the literature ($a = 1$, $m = 2.4$, $n = 2.0$). If we normalize the derived gas hydrate saturations in Fig. 6.5b with the saturation estimates outside the seeps, we still may expect up to 60% gas hydrate saturation for the most anomalous seep sites Piwakawaka and North Tower, ∼20% free gas and gas hydrate at Pukeko and only minor saturations at Riroriro. Gas hydrates may also exist, however, outside the seep areas.

The second case study is from the Danube delta fan, offshore western Black Sea. The Black Sea is a quasi-closed sea with kilometer-thick sediment layers. Anoxic conditions

have favored the production of methane (Reeburgh et al. 1991) and the formation of widespread gas hydrate provinces (Kessler et al. 2006). Sea level lowstands during the last glacial maximum led to high seafloor temperatures and extended fresh-water phases at most shelf regions, which have not equilibrated today (Soulet et al. 2010). The presence of gas hydrates within the stability field has been inferred from massive seafloor venting all along the continental edge of the gas hydrate stability field (e.g., Naudts et al. 2006; Schmale et al. 2011; Riboulot et al. 2017), direct sampling (Vassilev and Dimitrov 2002; Riboulot et al. 2018) and widespread BSR occurrences in seismic data (Lüdmann et al. 2004; Popescu et al. 2006; Baristeas 2006; Zander et al. 2017).

Figure 6.6a shows the resistivity model derived from the 2D CSEM inversion of a profile across the so-called S1 channel, which is one of the older channel levee systems of the offshore Danube fan. By using the same color scale as for the New Zealand model in Fig. 6.6a, the overall much higher resistivities become evident. As mentioned above, this is partly attributed to the much fresher pore water at depths below 40 m below seafloor (2.9 Ωm compared to 0.3 Ωm in New Zealand). The resistivity model also shows zonation of more saline conductive sediment (1–3 Ωm) close to the seafloor (A) and a ~100–150 m thick layer of higher resistivities (20–30 Ωm) at intermediate depths (B), which terminates towards the eastern levee. At depth below ~300 m below seafloor (~1800 m below sea level)
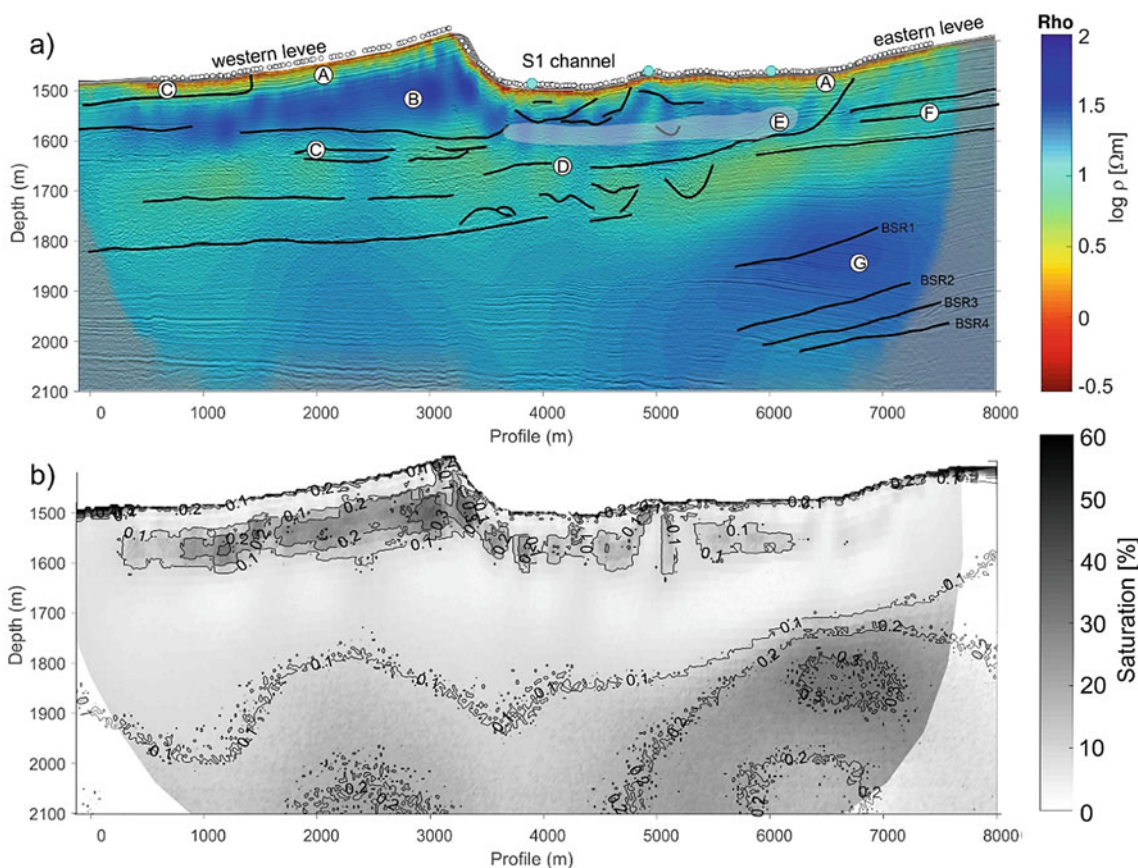

Fig. 6.6 a Resistivity model derived from 2D inversion of CSEM data from the offshore Danube fan, western Black Sea (Schwalenberg et al. 2020) overlaid on the 2D MCS section (Zander et al. 2017). The profile intersects the S1 channel, one of the older channel-levee systems of the offshore Danube fan. Interpretation of seismic and CSEM facies: (A) transition of conductive to more resistive sediment within the upper 40 mbsf; (B) a zone of fine grained homogeneously layered levee sediment below the western levee corresponds with high resistivity values (blue); (C) mass transport deposits of irregular seismic facies and amplitude variations occur close to the seafloor and, intercalated within deeper levee sediment, conform with lower resistivity values; (D) At intermediate depth below the S1 channel sediment are characterized by meandering sub channels caused by abundant levee failures and channel cuts; (E) a P-wave velocity anomaly (transparent) derived from OBS data (light blue dots, Bialas et al. 2020) correlates with a layer of high resistivities, which terminates towards the eastern levee where older levees are imaged by (F) strongly stratified sediment. (G) Resistivities increase towards a stack of multiple BSRs (Popescu et al. 2006; Zander et al. 2017) below the eastern levee. **b** Gas hydrate saturation model derived from the stochastic approach to Archie's equation after Sava and Hardage (2007), where the input parameters are represented by probability functions within appropriate parameter ranges. Transparency has been added to model parts of low sensitivity (Figure was modified from Schwalenberg et al. 2020)

resistivities rise again (~ 20 Ωm), particularly below the eastern levee (G).

The overlaid MCS section (Zander et al. 2017) provides further insight. High resistivities correlate with fine grained, homogeneously layered levee sediment below the western levee (B). Elevated resistivities within the channel (~ 20 Ωm) correlate with a low velocity zone (LVZ) derived from OBS data (E) (Bialas et al. 2020). Note: The OBS data covers only the S1 channel region, thus the LVZ may extend beneath the western levee. The deeper zone of high resistivities matches with a stack of multiple BSRs (Popescu et al. 2006; Baristeas 2006), which are characteristic for the area and possibly imply locally higher gas hydrate and free gas concentrations.

The saturation model in Fig. 6.6b has been calculated from the stochastic approach (Sava and Hardage 2007) to Archie's equation, where the input parameters are represented by probability functions randomly sampled within parameter ranges derived from nearby MeBo drilling (Riedel et al. 2020). This accounts for uncertainties in the input parameter. Figure 6.6b shows the median of the 68% confidence interval calculated for each grid element, which have uncertainties in the order of 15–20% given the range of input parameter (see Schwalenberg et al. 2020 for details). Seismic data show no indication of vertical fluid flow or gas migration into the GHSZ. Saturations around 10% below the S1 channel agree with the 6–12% pore filling gas hydrates levels that Dannowski et al. (2017) derived from OBS data. Below the western levee, gas hydrate saturation levels in the order of 20–30% seem unlikely within the layer of fine-grained sediment with reduced porosity and permeability (B) but may be present to a minor extent. This could be clarified with the help of seismic velocity information and drilling data, which are not available for this part of the profile. We explain high resistivities and elevated saturation estimates of 10–20% below the eastern levee with gas hydrates above and free gas below the BSRs.

6.7 Discussion and Conclusions

In the last two decades, marine CSEM methods have been applied to an increasing number of gas hydrate field studies all over the world (Fig. 6.3). These CSEM surveys have always been accompanied or guided by reflection seismic surveys, and in some cases also by deep ocean drilling (numbers 1, 2, 4, and 9 in Fig. 6.3). Resistivity studies add valuable information regarding the nature of the pore fluid. Resistive gas hydrate and free gas can be clearly distinguished from conductive saline pore fluid. Ambiguity remains in distinguishing between free gas, gas hydrate and other sediment properties such as carbonates and lithology changes, as these parameters are difficult to measure based on CSEM data alone. This ambiguity can be reduced by seismic velocity data, for example, which measure higher in hydrate-rich zones and lower where free gas is present (e.g., below the base of gas hydrate stability), and are thus also used to derive saturation estimates. Reflection seismic data provide the necessary insight into the sediment stratigraphy and lithology sequence imaging channels and faults where gas can migrate into the GHSZ, forming gas hydrate. While already small amounts of free gas and gas hydrates may cause blanking and the scattering of seismic energy, low saturation levels of less than 5–10% may remain unresolved from the resistivity data, which emphasize the ability of CSEM methods to identify highly saturated gas hydrate deposits. The common and widely used method to calculate saturation estimates is based on Archie's equation (Archie 1942). Originally introduced for clean sands, it has been widely debated to what extent Archie's equation provides reliable estimates, not only of the gas hydrate saturation levels, but generally in the hydrocarbon industry (e.g., Worthington 1993; Waite et al. 2009). Constraints on the input parameter of Archie's equation, particularly porosity, pore fluid salinity, cementation factor and saturation exponent, are therefore vital for accurate saturation estimates.

Prior to calculating saturation estimates, resolution and sensitivity studies should be applied to the CSEM resistivity models, showing to what extent the model is supported by the data. Error analyses of the saturation estimates and stochastic methods using probability functions further address the problem (Schwalenberg et al. 2020). Collocated seismic and CSEM data allow for accurate saturation estimates, applying joint elastic-electrical effective medium modelling (Ellis et al. 2008b; Attias et al. 2020).

Seafloor drilling provides the necessary in-situ physical parameters, which are important to calibrate the physical models. However, the scale problem between in-situ drilling and remote sensing methods should be considered when jointly interpreting the data.

The two case studies presented demonstrate how seismic and CSEM data complement each other. The CSEM study on Opouawe Bank points at significant gas hydrate deposits below the seeps, which was not made clear by the seismic data alone. The joint interpretation of CSEM and seismic data of the S1 channel levee system of the offshore Danube fan helped to classify the nature of the resistivity anomalies and to distinguish between possible gas hydrate accumulations and lithology-driven changes. For further aspects and insights that CSEM methods provide for submarine gas hydrate investigations, we refer the reader to the case studies cited in Fig. 6.3.

References

Archie GE (1942) The electrical resistivity log as an aid in determining some reservoir characteristics. Pet Trans AIME 146:54–62

Attias E, Weitemeyer K, Minshull TA et al (2016) Controlled-source electromagnetic and seismic delineation of subseafloor fluid structures in a gas hydrate province offshore Norway. Geophys J Int 206:1093–1110. https://doi.org/10.1093/gji/ggw188

Attias E, Weitemeyer K, Hölz S et al (2018) High-resolution resistivity imaging of marine gas hydrate structures by combined inversion of CSEM towed and ocean-bottom receiver data. Geophys J Int 214:1701–1714

Attias E, Amalokwu K, Watts M et al (2020) Gas hydrate quantification at a pockmark offshore Norway from joint effective medium modelling of resistivity and seismic velocity. Mar Pet Geol 113:104151

Avdeeva A, Commer M, Newman GA (2007) Hydrocarbon reservoir detectability study for marine CSEM methods: time domain versus frequency domain. In: SEG technical program expanded abstracts 2007, Soc Explor Geophys, pp 628–632

Baba K (2005) Electrical structure in marine tectonic settings. Surv Geophys 26:701–731

Baristeas N (2006) Seismische Fazies Tektonik und Gashydratvorkommen im nordwestlichen Schwarzen Meer. Diplomarbeit, Universität Hamburg, Germany, p 106

Barnes PM, Lamarche G, Bialas J et al (2010) Tectonic and geological framework for gas hydrates and cold seeps on the Hikurangi subduction margin, New Zealand. Mar Geol 272(1–4):26–48

Bialas J, Bohlen T, Dannowski A et al (2020) Joint interpretation of geophysical field experiments in the Danube deep sea fan, Black Sea. Mar Pet Geol 121:104551

Bialas J, GreinertJ, Linke P et al (eds) (2007) RV SONNE Cruise Report SO191—New Vents Puaretanga Hou, 11.01.–23.03.2007, Wellington–Napier–Auckland, (Cruise Report No 09), Kiel, Germany. Berichte aus dem Leibniz-Institut für Meereswissenschaften an der Christian-Albrechts-Universität zu Kiel. ISSN Nr 1614-6298

Bialas J (ed) (2011) RV SONNE Cruise Report SO214—NEMESYS, 09.03.–05.04.2011, Wellington–Wellington, 06.–22.04.2011, Wellington–Auckland (Cruise Report No 47), Kiel, Germany. Berichte aus dem Leibniz-Institut für Meereswissenschaften an der Christian-Albrechts-Universität zu Kiel. ISSN Nr 1614-6298

Bünz S, Polyanov S, Vadakkepuliyambatta S et al (2012) Active gas venting through hydrate-bearing sediments on the Vestnesa Ridge, offshore W-Svalbard. Mar Geol 332:189–197

Collett TS, Ladd J (2000) Detection of gas hydrate with downhole logs and assessment of has hydrate concentrations (saturations) and gas volumes on the Blake Ridge with electrical resistivity log data. In: Paull CK, Matsumoto R, Wallace PJ et al (eds) Proc Ocean Drill Prog Sci Res, vol 164

Connell D, Key K (2013) A numerical comparison of time and frequency-domain marine electromagnetic methods for hydrocarbon exploration in shallow water. Geophys Prospect 61:187–199

Constable S (2013) Instrumentation for marine magnetotelluric and controlled source electromagnetic sounding. Geophys Prospect 61:505–532

Constable SC, Parker RL, Constable CG (1987) Occam's inversion: a practical algorithm for generating smooth models from electromagnetic sounding data. Geophysics 52(3):289–300

Constable S, Kannberg PK, Weitemeyer K (2016) Vulcan: a deep-towed CSEM receiver. Geochem Geophys 17:1042–1064. https://doi.org/10.1002/2015GC006174

Constable S (2010) Ten years of marine CSEM for hydrocarbon exploration. Geophysics 75(5):75A67–75A81

Cook AE, Waite WF (2018) Archie's saturation exponent for natural gas hydrate in coarse-grained reservoirs. J Geophys Res Solid Earth 123(3):2069–2089

Crutchley GJ, Fraser DRA, Pecher IA et al (2015) Gas migration into gas hydrate-bearing sediments on the southern Hikurangi margin of New Zealand. J Geophys Res Solid Earth 120(2):725–743

Dannowski A, Bialas J, Schwalenberg K et al (2017) Shear wave modelling of high resolution OBS data with a comparison to CSEM data in a gas hydrate environment in the Danube deep-sea fan, Black Sea. Presented at the 9th International Conference on Gas Hydrates, Denver, US, June 25–30 2017

Duan S, Hölz S, Jegen M et al (2021) Study on gas hydrate targets in the Danube delta with the sputnik controlled-source electromagnetic system. Mar Pet Geol (under revision)

Edwards RN (1997) On the resource evaluation of marine gas hydrate deposits using sea-floor transient electric dipole-dipole method. Geophysics 62(1):63–74

Edwards RN (2005) Marine controlled source electromagnetics: principles, methodologies, future commercial applications. Surv Geophys 26:675–700

Ellingsrud S, Eidesmo T, Johansen S et al (2002) Remote sensing of hydrocarbon layers by seabed logging (SBL): results from a cruise offshore Angola. Lead Edge 21(10):972–982

Ellis M, Evans R, Hutchinson D et al (2008) Electromagnetic surveying of seafloor mounds in the northern Gulf of Mexico. Mar Pet Geol 25 (9):960–968. https://doi.org/10.1016/j.marpetgeo.2007.12.006

Ellis M, Minshull TA, Sinha MC et al (2008b) Joint seismic/electrical effective medium modelling of hydrate-bearing marine sediments and an application to the Vancouver Island Margin. In: Proceedings of the 6th international conference on gas hydrates (ICGH 2008), Vancouver, British Columbia, CANADA, July 6–10 2008

Evans RL (2007) Using CSEM techniques to map the shallow section of seafloor: from the coastline to the edges of the continental slope. Geophysics 72:105–116

Filloux JH (1987) Instrumentation and experimental methods for oceanic studies. In: Jacobs JA (ed) Geomagnetism. Academic Press, pp 143–248

Flosadottir AH, Constable S (1996) Marine controlled-source electromagnetic sounding: 1. Modeling and experimental design. J Geophys Res Solid Earth 101(B3):5507–5517

Fofonoff NP (1985) Physical Properties of seawater: a new salinity scale and equation of state for seawater. J Geophys Res 90:3332–3342

Gehrmann RAS, Schwalenberg K, Riedel M et al (2016) Bayesian inversion of marine controlled source electromagnetic data offshore Vancouver Island, Canada. Geophys J Int 204:21–38

Goswami BK, Weitemeyer KA, Minshull TA et al (2015) Resistivity image beneath an area of active methane seeps in the west Svalbard continental slope. Geophys J Int 207:1286–1302

Goswami BK, Weitemeyer KA, Minshull TA et al (2016) A joint electromagnetic and seismic study of an active pockmark within the hydrate stability field at the Vestnesa Ridge, West Svalbard margin. J Geophys Res Solid Earth 120:6797–6822. https://doi.org/10.1002/2015JB012344

Goto T, Kasaya T, Machiyama H et al (2008) A marine deep-towed DC resistivity survey in a methane hydrate area, Japan Sea. Explor Geophys 39:52–59

Greinert J, Lewis K, Bialas J et al (2010) Methane seepage along the Hikurangi Margin, New Zealand: overview of studies in 2006 and 2007 and new evidence from visual, bathymetric and hydroacoustic investigations. Mar Geol 272(1–4):6–25

Henrys S, Ellis S, Uruski C (2003) Conductive heat flow variations from bottom simulating reflectors on the Hikurangi margin. NZ Geophys Res Lett 30(2):1065–1068

Hsu S-K, Chiang C-W, Evans RL et al (2014) Marine controlled source electromagnetic method used for the gas hydrate investigation in the offshore area of SW Taiwan. J Asian Earth Sci 92:224–232

Jackson PD, Taylor Smith D, Stanford PN (1978) Resistivity-porosity-particle shape relationships for marine sands. Geophysics 43(6):1250–1268

Jegen M, Hoelz S, Swidinsky A et al (2014) Electromagnetic and seismic investigation of methane hydrates offshore Taiwan—the Taiflux experiment. In: OCEANS 2014-TAIPEI, IEEE, pp 1–4

Jing JE, Chen K, Deng M et al (2019) A marine controlled-source electromagnetic survey to detect gas hydrates in the Qiongdongnan Basin, South China Sea. J Asian Earth Sci 171:201–212

Kannberg PK, Constable S (2020) Characterization and quantification of gas hydrates in the California Borderlands. Geophys Res Lett 47: e2019GL084703

Kessler JD, Reeburgh WS, Southon J et al (2006) Basin-wide estimates of the input of methane from seeps and clathrates to the Black Sea. Earth Planet Sci Lett 243:366–375

Key K (2016) MARE2DEM: a 2-D inversion code for controlled-source electromagnetic and magnetotelluric data. Geophys J Int 207(1):571–588

Key K, Constable S (2021) Inverted long-baseline acoustic navigation of deep-towed CSEM transmitters and receivers. Mar Geophys Res 42(1):1–15

Klaucke I, Weinrebe W, Petersen CJ et al (2010) Temporal variability of gas seeps offshore New Zealand: multi-frequency geoacoustic imaging of the Wairarapa area, Hikurangi margin. Mar Geol 272:49–58

Koch S, Schroeder H, Haeckel M et al (2016) Gas migration through Opouawe Bank at the Hikurangi margin offshore New Zealand. Geo Mar Lett 36(3):187–196. https://doi.org/10.1007/s00367-016-0441

Kretschmer K, Biastoch A, Rüpke L et al (2015) Modeling the fate of methane hydrates under global warming. Glob Biogeochem Cycles 29:610–625. https://doi.org/10.1002/2014GB005011

Lee MW, Collett TS (2006) A method of shaly sand correction for estimating gas hydrate saturations using downhole electrical resistivity log data, vol 5121. US Department of the Interior, US Geological Survey

Lewis KB, Marshall BA (1996) Seep faunas and other indicators of methane-rich dewatering on New Zealand convergent margins. NZ J Geol Geophys 39:181–200

Liu X, Flemings PB (2006) Passing gas through the hydrate stability zone at southern Hydrate Ridge, offshore Oregon. Earth Planet Sci Lett 241(1–2):211–226

Lüdmann T, Wong HK, Konerding P et al (2004) Heat flow and quantity of methane deduced from a gas hydrate field in the vicinity of the Dnieper Canyon, Northwestern Black Sea. Geo Mar Lett 24 (3):182–193

McDougall TJ, Barker PM (2011) Getting started with TEOS-10 and the Gibbs Seawater (GSW) oceanographic toolbox. SCOR/IAPSO WG 127:1–28

Mir R, Edwards N (2011) The assessment and evolution of offshore gas hydrate deposits using seafloor controlled source electromagnetic methodology. In: SEG technical program expanded abstracts, vol 30 (1), pp 682–686. https://doi.org/10.1190/1.3628170

Mir R (2011) Design and deployment of a controlled source EM instrument on the NEPTUNE observatory for long-term monitoring of methane hydrate deposits. PhD thesis, University of Toronto

Myer D, Constable S, Key K (2011) Broad-band waveforms and robust processing for marine CSEM surveys. Geophys J Int 184:689–698

Nabighian MN (ed) (1991) Electromagnetic methods in applied geophysics, vol 2, Application, Parts A and B. Society of Exploration Geophysicists

Naudts L, Greinert J, Artemov Y et al (2006) Geological and morphological setting of 2778 methane seeps in the Dnepr paleo-delta, Northwestern Black Sea. Mar Geol 227(3–4):177–199

Ocean Floor Geophysics (2014) Ocean floor geophysics completes CSEM gas hydrate survey in Japan. OFG Press Release. http://www.oceanfloorgeophysics.com/news?-offset=1485156274175. Accessed 23 Oct 2014

Ocean Floor Geophysics (2015) Another CSEM gas hydrate survey completed in Japan. OFG Press Release. http://www.oceanfloorgeophysics.com/news?-offset=1536206743526. Accessed 1 Sep 2015

Ocean Floor Geophysics (2018) Another major gas hydrate CSEM mapping campaign completed in Japan. OFG Press Release. http://www.oceanfloorgeophysics.com/news?-offset=1536206743526. Accessed 26 April 2018

Pearson CF, Halleck PM, McGuire PL et al (1983) Natural gas hydrate deposits: a review of insitu properties. J Phys Chem 87:4180–4185

Pecher IA, Henrys SA, Zhu H (2004) Seismic images of gas conduits beneath vents and gas hydrates on Ritchie Ridge, Hikurangi margin, New Zealand. NZ J Geol Geophys 47:275–279

Popescu I, DeBatist M, Lericolais G et al (2006) Multiple bottom simulating reflectors in the Black Sea: potential proxies of past climate conditions. Mar Geol 227:163–176

Ray A, Alumbaugh DL, Hoversten GM et al (2013) Robust and accelerated Bayesian inversion of marine controlled-source electromagnetic data using parallel tempering. Geophysics 78(6):E271–E280

Reeburgh WS, Ward BB, Whalen SC et al (1991) Black Sea methane geochemistry. Deep Sea Res Part A Ocean Res Pap 38(2):S1189–S1210

Riboulot V, Cattaneo A, Scalabrin C et al (2017) Control of the geomorphology and gas hydrate extent on widespread gas emissions offshore Romania. Bulletin De La Société Géologique De France 188(4):26

Riboulot V, Ker S, Sultan N et al (2018) Freshwater lake to salt-water sea causing widespread hydrate dissociation in the Black Sea. Nat Commun 9:117

Riedel M, Spence GD, Chapman NR et al (2002) Seismic investigations of a vent field associated with gas hydrates, offshore Vancouver Island. J Geophys Res Solid Earth 107(B9):EPM-5

Riedel M, Freudenthal T, Bergenthal M et al (2020) Physical properties, in situ temperature, and core-log seismic integration at the Danube Deep-Sea Fan, Black Sea. Mar Pet Geol 114:104192

Ruppel CD, Kessler JD (2017) The interaction of climate change and methane hydrates. Rev Geophys 55:126–168

Salem HS, Chilingarian GV (1999) The cementation factor of Archie's equation for shaly sandstone reservoirs. J Pet Sci Eng 23:83–93

Sava DC, Hardage BA (2007) Gas-hydrate concentration and uncertainty estimation from electrical resistivity logs: examples from Green Canyon, Gulf of Mexico. In: SEG technical program expanded abstracts 2007, pp 1–4

Schmale O, Haeckel M, McGinnis DF (2011) Response of the Black Sea methane budget to massive short-term submarine inputs of methane. Biogeosciences 8:911–918

Schwalenberg K, Willoughby EC, Mir R et al (2005) Marine gas hydrate electromagnetic signatures in Cascadia and their correlation with seismic blank zones. First Break 23:57–63

Schwalenberg K, Haeckel M, Poort J et al (2010) Evaluation of gas hydrate deposits in an active seep area using marine controlled source electromagnetics: results from Opouawe Bank, Hikurangi Margin, New Zealand. Mar Geol 272(1–4):79–88

Schwalenberg K, Rippe D, Koch S et al (2017) Marine-controlled source electromagnetic study of methane seeps and gas hydrates at

Opouawe Bank, Hikurangi Margin, New Zealand. J Geophys Res Solid Earth 122:3334–3350

Schwalenberg K, Yuan J, Edwards N et al (2004) Marine controlled source electromagnetic experiments to evaluate gas hydrates off the coastlines of North and South America. In: Extended abstract, Marelec conference 17–18.03.2004. London, pp 1–13

Schwalenberg K, Gehrmann RAS, Bialas J et al (2020) Analysis of marine controlled source electromagnetic data for the assessment of gas hydrates in the Danube deep-sea fan, Black Sea. Mar Pet Geol 120.https://doi.org/10.1016/j.marpetgeo.2020.104650

Sherman D, Kannberg P, Constable S (2017) Surface towed electromagnetic system for mapping of subsea Arctic permafrost. Earth Planet Sci Lett 460:97–104

Sinha MC, Patel PD, Unsworth MJ et al (1990) An active source electromagnetic sounding system for marine use. Mar Geophys Res 12(1–2):59–68

Soulet G, Delaygue G, Vallet C et al (2010) Glacial hydrologic conditions in the Black Sea reconstructed using geochemical pore water profiles. Earth Planet Sci Lett 296(1–2):57–66

Spangenberg E (2001) Modeling of the influence of gas hydrate content on the electrical properties of porous sediments. J Geophys Res 106:6535–6548

Tikhonov AN, Arsenin VY (1977) Solutions of ill-posed problems. Wiley

Tréhu AM, Bohrmann G, Torres ME et al (eds) (2006) Proceeding ODP, Scientific Results 204, College Station, TX (Ocean Drilling Program)

Vassilev A, Dimitrov LI (2002) Spatial and quantity evaluation of the Black Sea gas hydrates. Russ Geol Geophys 43:672–684

Waite WF, Santamarina JC, Cortes DD et al (2009) Physical properties of hydrate-bearing sediments. Rev Geophys 47:RG4003. https://doi.org/10.1029/2008RG000279

Wang M, Deng M, Zhao Q et al (2015) Two types of marine controlled source electromagnetic transmitters. Geophys Prospect 63:1403–1419

Wang L, Xiong S, Li Y et al (2019) Evaluation of gas hydrate structures: results from an experiment in the South China Sea using the marine controlled-source electromagnetic method. Bollettino di Geofisica Teorica ed Applicata 60(4)

Ward SH, Hohmann GW (1988) Electromagnetic theory for geophysical applications. In: Nabighian NM (ed) Electromagnetic methods in applied geophysics. Soc Explor Geophys 131–311

Weitemeyer K, Constable S (2010) Mapping shallow seafloor structure with marine CSEM, examples from the Gulf of Mexico gas hydrate experiment. First Break 6(28):97–102

Weitemeyer KA, Constable SC, Key KW et al (2006) First results from a marine controlled-source electromagnetic survey to detect gas hydrates offshore Oregon. Geophys Res Lett 33:L03304. https://doi.org/10.1029/2005GL024896

Weitemeyer K, Constable S, Shelander D et al (2017) Mapping the resistivity structure of Walker Ridge 313 in the Gulf of Mexico using the marine CSEM method. Mar Pet Geol 88:1013–1031

Weitemeyer KA, Constable S, Trehu AM (2011) A marine electromagnetic survey to detect gas hydrate at Hydrate Ridge, Oregon. Geophys J Int 187(1):45–62. https://doi.org/10.1111/j.1365-246X.2011.05105.x

Winsauer WO, Shearin HM, Masson PH et al (1952) Resistivity of Brine saturated sands in relation to pore geometry. Am Assoc Pet Geol Bull 36(2):253–277

Worthington PF (1993) The uses and abuses of the Archie equations, 1: the formation factor-porosity relationship. J Appl Geophys 30:215–228

Yuan J, Edwards RN (2000) The assessment of marine gas hydrates through electrical remote sounding: hydrate without a BSR? Geophys Res Lett 27:2397–2400

Zander T, Haeckel M, Berndt C et al (2017) On the origin of multiple BSRs in the Danube deep-sea fan, Black Sea. Earth Planet Sci Lett 462:15–25